Electronic Supplementary Material (ESI) for ChemComm.
This journal is © The Royal Society of Chemistry 2019

Supporting Online Material for

Resistive switching in an organic supramolecular semiconducting ferroelectric

Nicolás M. Casellas, [a, b] Indre Urbanaviciute, [d] Tim Cornelissen, [d] José Augusto Berrocal,[e]
Tomás Torres,* [a, b, c] Martijn Kemerink, * [d] Miguel García-Iglesias.*,[a, b]

[a] Department of Organic Chemistry, Universidad Autónoma de Madrid (UAM), Calle Francisco Tomás y Valiente, 7, 28049 Madrid, ES. E-mail: tomas.torres@uam.es, miguel.iglesias@uam.es. [b] IMDEA Nanociencia, c/ Faraday 9, Cantoblanco, 28049, ES. [c] Institute for Advanced Research in Chemical Sciences (IAdChem), UAM, 28049 Madrid, ES. [d] Complex Materials and Devices, Department of Physics, Chemistry and Biology (IFM), Linköping University, 58183 Linköping, Sweden. E-mail: martijn.kemerink@liu.se. [e] Institute for Complex Molecular Systems, Eindhoven University of Technology, P. O. Box 513, 5600 MB Eindhoven, The Netherlands.

Contents

I. Synthetic procedures

Motivation

Semiconducting-ferroelectric discotic molecules reported before demonstrated unique resistive switching behaviour yet demanded cumbersome synthetic procedures.[1] Therefore a simpler, efficient synthetic approach resulting in similar or better materials was highly desired. The synthesis of **BTTTA** is straightforward and efficient facilitating affording the desired product in a multigram scale, see below for details. The molecule comprises three equally important structural parts – a π-stacking semiconducting BTT core to which three free-to-rotate dipolar amide groups are attached, followed by a single linear alkyl chain. While the conjugated cores and H-bonding amide groups induce strong self-assembly in one-dimensional axial aggregates and stabilize the supramolecular structure, the flexible dodecyl chains supply enough molecular mobility, *e.g.* for the columnar macrodipole to be switched. From the application perspective, a successful ferroelectric operation of devices based on liquid-crystalline discotics is determined by the homeotropic alignment level, which requires certain level of molecular mobility at elevated (processing) temperatures. This can be achieved by phase diagram engineering through molecular structure modifications. Inspiration for the rational design of the **BTTTA** was taken from the structure-property relation studies on an archetypal columnar discotic ferroelectric benzene-1,3,5-tricarboxamide BTA [2,3] as well as materials comprising larger (sub)phthalocyanine, perylene bisimide and carbonyl-bridged triarylamine cores, as discussed in the introduction of the main text. Large cores and bulky sidechains of previously reported semiconducting molecules impeded homeotropic alignment, which is solved here by an optimal choice of a smaller BTT core and unbranched dodecyl sidechains. This facilitated homeotropic alignment, enabling larger and higher quality self-assemblies, led to significantly increased charge transport mobilities and strongly suppressed depolarization in **BTTTA**, compared to its predecessors with polarization retention of several minutes at elevated temperatures. The resistive switching behavior is largely dependent on strong ferroelectric-semiconductor coupling in a material. In multifunctional molecules like **BTTTA** this is essentially determined by the spatial proximity of the dipolar moieties and the charge transport channel (=conjugated core) in the supramolecular structure. Compared to the previously synthesized similar type materials, the optimized structure of **BTTT**A satisfies this condition and assures minimal separation between these active elements. Summarizing, the rational design of the **BTTTA** solved several weaknesses of previously synthesized analogous materials and can be considered the best choice so far for memory applications based on different types of resistive switching.

Materials

Chemicals were purchased from commercial suppliers (SIGMA Aldrich) and used without further purification unless stated otherwise. Dry THF was degassed and obtained after passage through an activated alumina solvent column system. Column chromatography was carried out on silica gel (Merk, kieselgel 60, 230-400 mesh, 60 Å). Reactions were followed by thin-layer chromatography on aluminium sheets precoated 0.25 mm, 60-F254 silica gel plates from Merck. Reactions were performed under an atmosphere of dry argon unless stated otherwise.

Methods

^{1}H-NMR and ^{13}C-NMR spectra were recorded on a Bruker AC-300 or a Bruker AC-500 spectrometer. Chemicals shifts are given in ppm (δ) values relative to residual solvent or tetramethylsilane (TMS). Splitting patterns are labeled as s, singlet; d, doublet; dd, double doublet; t, triplet; q, quartet; quin, quintet; m, multiplet and b stands for broad. MS (MALDI-TOF) spectra were performed on a BRUKER REFLEX III instrument that was equipped with a nitrogen laser operating at 337 nm and recorded in the positive-polarity mode. High-resolution spectra were acquired using a 9.4 T IonSpec QFT-MS FT-ICR mass spectrometer. Some samples were analyzed in a mass spectrometer with hybrid analyzer QTOF model MAXIS II of the commercial house Bruker. An Acquity UPLC from the commercial house Waters was used as an entryway in Flow Injection analysis mode (FIA).

Synthetic protocols and characterization

The synthetic route of **BTTTA** is depicted in ***Scheme 1***.

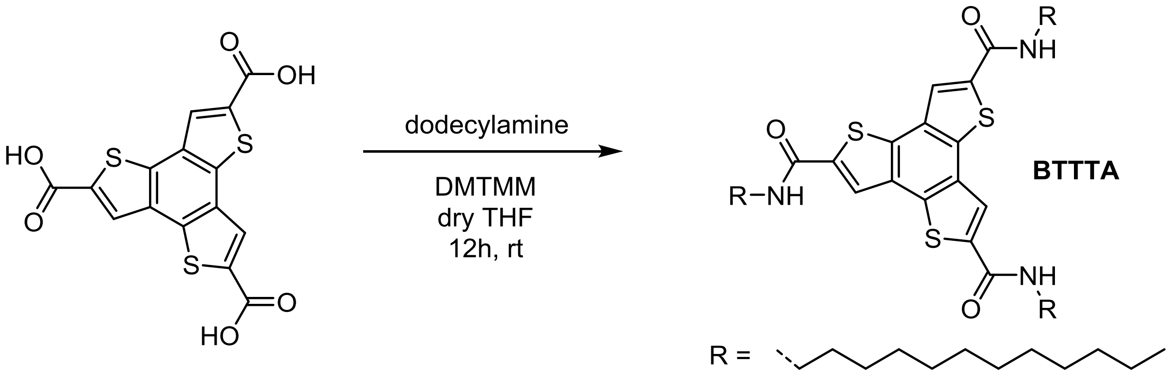

Scheme 1: Dodecylamine, 4-(4,6-Dimethoxy-1,3,5-triazin-2-yl)-4-methylmorpholinium chloride (DMTMM), THF, R.T, 12h, 80%.

Synthetic protocol for the benzotrithiophene tricarboxamide BTTTA

Benzo-(1,2;3,4;5,6)-tris(thiophene-2'-carboxylic acid (5.0 g, 13.2 mmol)[3], DMTMM (16.7 g, 60.4 mmol) in dry THF (1 L) and dodecylamine **1** (9.0 g, 62.8 mmol) were added to a round bottom flask under argon atmosphere. The reaction was stirred for 12 h at room temperature. Subsequently, the solvent was removed in vacuo. The material was dissolved in chloroform and washed with $NaHCO_3$ solution, HCl (1%) solution and water. The organic phases were dried over anhydrous $MgSO_4$. After solvent removal, the solid was filtered yielding **BTTTA**, 10.2 g (80%) as a white solid.

^{1}H-NMR (300 MHz, DMSO-*d6*) δ (ppm) 8.86 (s, 3H, NH), 8.49 (s, 3H, core), 1.65-1.50 (m, 6H, CH_2NH), 1.38-1.19 (m, 60H, CH_2), 0.85-0.79 (m, 9H, CH_3). **^{13}C-NMR** (126MHz, DMSO-*d6*) δ (ppm) 160.40, 140.12, 134.09, 130.62, 122.02, 30.71, 28.46, 28.43, 28.41, 28.38, 28.19, 28.07, 25.98, 21.43, 13.18. **FT-IR** (ATR) υ (cm^{-1}): 3243.016, 2952.030, 2923.606, 2866.371, 1625.786, 1544.639, 1464.572, 1361.816, 1295.974, 1237.870, 837.821. **MS** (MALDI-TOF, Ditranol): m/z = 880.6 $[M+H]^+$ (100%). HR-MS (MALDI, matrix DCTB + PPGNa 790): m/z 880.5505 $[M+H]^+$ (calculated: 880.5513).

Supporting data

^{1}H-NMR of BTTTA (DMSO-*d6*)

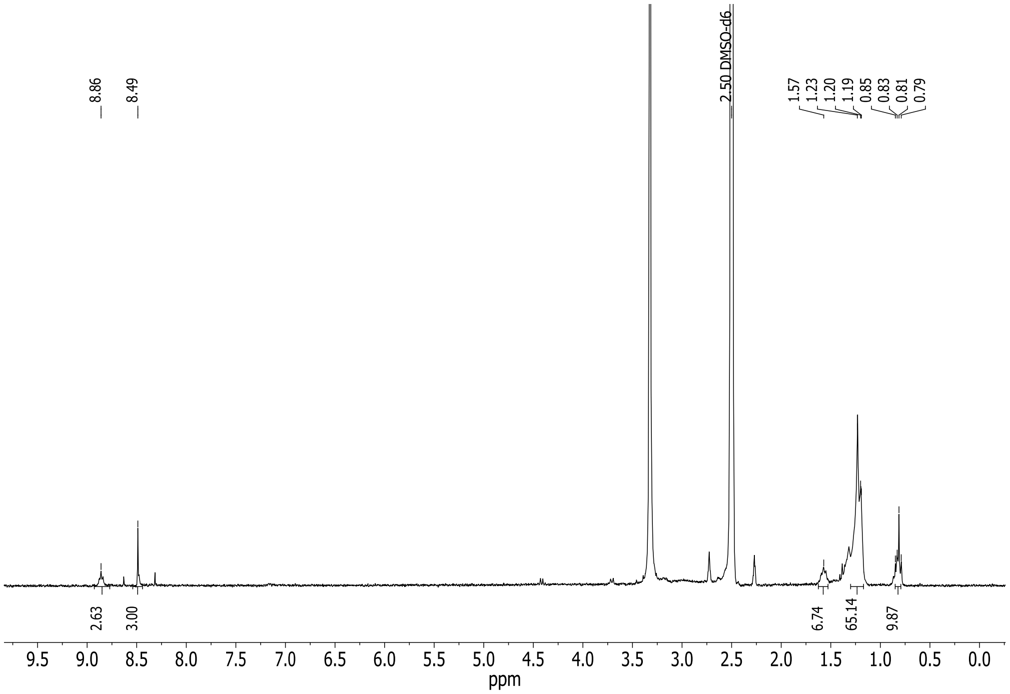

^{13}C-NMR of BTTTA (DMSO-*d6*)

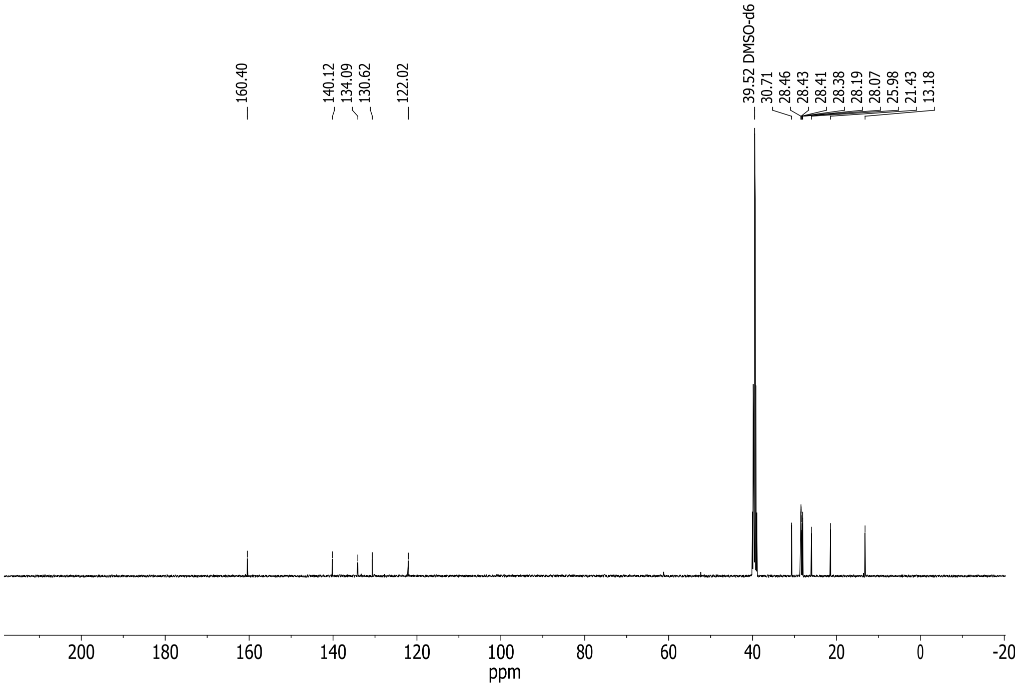

FT-IR spectrum of BTTTA in solid state

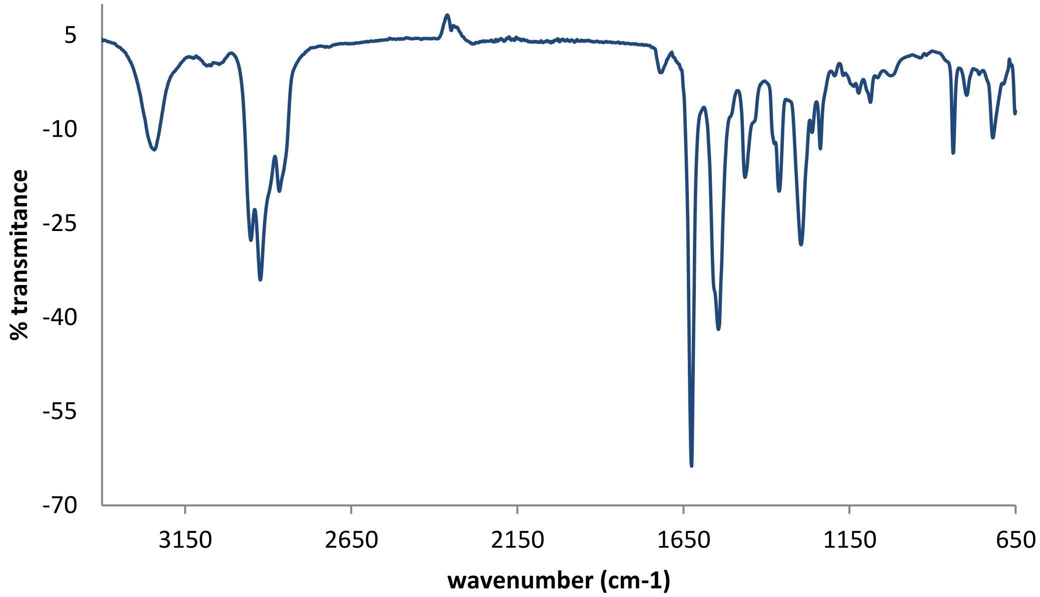

MALDI-TOF spectra with (inset) isotopic distribution pattern HR-MALDI-TOF spectrum of BTTTA.

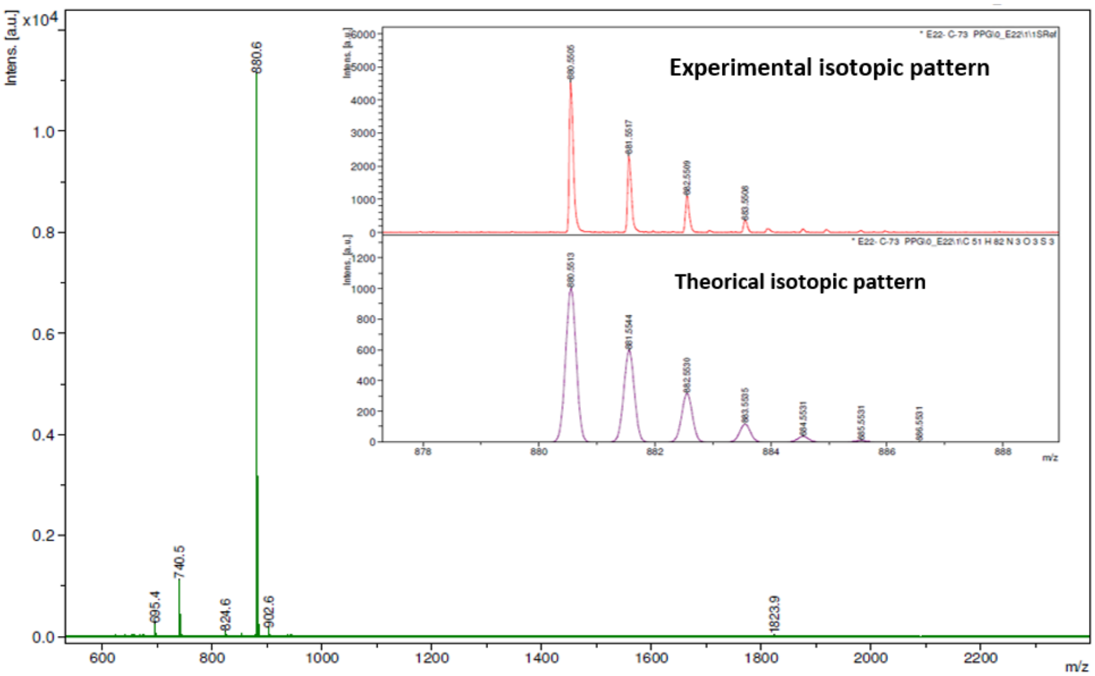

II. Device fabrication and conditioning

Thin film metal-ferroelectric-metal (MFM) capacitor devices were formed by spin-coating (500–1500 rpm) of a 10–30 mg/ml chloroform solution on a chemically cleaned glass substrate with patterned metal bottom electrodes. Before thermal vacuum deposition of the metal top electrodes, spin-coated films were annealed at ~70 °C for 5 min. to completely evaporate the solvent. The prepared MFM devices were 0.01–1 mm^2 in area. Typical film thickness was 300–800 nm, as measured by a Bruker Dektak XT profilometer.

In-plane gold and platinum interdigitated electrode substrates with 5 µm electrode width, 5 µm gap between the electrodes and 180 electrode pairs were purchased from Micrux Technologies. Gold and platinum electrodes (150 nm) are sputtered on glass with titanium (50 nm) adhesion layer. Total electrode area is 0.1924 mm^2, device area under illumination is 4.81 mm^2. Devices were cleaned in deionized water, acetone and isopropanol ultrasound bath followed by blow-drying with nitrogen after each cleaning step. The active material was then spin-coated at 2000 rpm and annealed at 70°C for 5 min. for complete solvent removal.

In the as-cast organic ferroelectric film molecular columns lie randomly in-plane to the electrode. When molecular dipoles are oriented in this way, no polarization can be measured in the bottom-top electrode geometry. Therefore, prior to the electrical measurements the devices are treated by a short field-annealing procedure, when at low viscosity conditions (>100 °C) with the help of an alternating external field molecular bundles are forced to stand perpendicularly to the electrodes. The followed field cooling freezes the system in this quasi-orderly state. Due to π-stacking of the conjugated cores and hydrogen bonding of the amide groups, accompanied by alkyl chain freezing, the packing remains stable even without external field.

III. Electrical characterization

The ferroelectric polarization loops are obtained by integration of the switching current transients. We use a quasi-static mode, better known as the Double Wave Method (DWM), when the non-switching current is subtracted from the initial signal to avoid displacement and leakage inputs in the *P*-*E* curves. The input signal waveform is supplied by a Tektronix AFG3000 Arbitrary Function Generator and is amplified by a TREK PZD350A high voltage amplifier. The device response is visualized by a Tektronix TBS1000B Digital Oscilloscope.

The polarization retention measurement is performed in a similar manner as the other electrical characterization, the only difference being the waiting time between the poling and probing triangular signals. The devices are left at short circuit conditions during the waiting time. Each data point is measured after full repolarization.

Switching kinetics is obtained from a step response measurement. The device is fully (negatively) poled and transient switching current is measured as a response to a (positive) square input signal. The amplitude of the probing step is gradually changed, while conditioning step amplitude is kept constant. The non-switching current (electrical displacement and (possible) leakage current) is measured and later subtracted, similarly to the DWM protocol.

Capacitance-voltage characteristics are measured by a Zurich Instruments Mid-frequency impedance analyzer (MFIA).

Static *j*-*V* curves were obtained by a Keithley 2636B SourceMeter SMU.

All electrical measurements were performed in dark.

IV. Other characterization

FT-IR spectrometer, equipped with a temperature controller Pike GladiATR EZ-ZONE PM. **Polarisation optical microscopy (POM)** measurements were done using a Jenaval polarisation microscope equipped with a Linkam THMS 600 heating device, with crossed polarizers.

The thermal transitions were determined with **DSC** using a Perkin–Elmer Pyris 1 DSC under a nitrogen atmosphere with heating and cooling rates of 10 K min^{-1}.

X-Ray scattering measurements were performed on a Ganesha lab instrument equipped with a GeniX-Cu ultra-low divergence source producing X-ray photons with a wavelength of 1.54 Å and a flux of 1 x 108 ph/s. Scattering patterns were collected using a Pilatus 300K silicon pixel detector with a 487 x 619 pixel dimension and with 172 μm^2 pixel size at 113 mm and 1513 mm sample to detector distance. The beam centre and the q range were calibrated using the diffraction peaks of silver behenate. Glass capillaries were filled with the material for the diffraction analysis and placed in a Linkam HFSX350 heating stage and measured at a range of 25 °C to +300 °C with 10 °C/min. Each pattern was recorded for 10 min. Azimuthal integration of the obtained diffraction patterns was performed by utilizing the SAXSGUI software.The peaks were fitted using a Lorentz peak, using a slope to correct for the background slope.

The surface topography of **spin-coated BTTTA films** has been studied by Veeco Dimension 3100 atomic force microscope in a tapping mode.

Ultraviolet-visible (UV-vis) absorbance spectra were recorded on a Jasco V-660-spectrophotometer and a using quartz cuvettes (1cm) or quartz substrates in the case of spin-coated films.

Cyclic Voltammetry (CV) and Square Wave Voltammetry (SWV): Electrochemical measurements were performed on an Autolab PGStat 30 equipment using a three electrode configuration system. The measurements were carried out using freshly distilled DCM solution containing 0.1 M tetrabutylammonium hexafluorophosphate ($TBAPF_6$) and a concentration of 10^{-4} M of the corresponding compound. A glassy carbon electrode (3 mm diameter) was used as the working electrode, and a platinum wire and an $Ag/AgNO_3$ (in CH_3CN) electrode were employed as the counter and the reference electrodes, respectively. Ferrocene (Fc) was used as an internal reference and all the potentials were given relative to the Fc/Fc$^+$ couple. Scan rate was 100 mV s^{-1} unless otherwise specified.

V. Small-signal characteristics

BTTTA demonstrates typical small-signal ferroelectric characteristics. The measured capacitance-voltage characteristics are butterfly-shaped with prominent peaks at the coercive field (Fig. S8b). When integrated, these *C*-*V* characteristics give reversible polarization hysteresis loops with polarization values that are significantly lower than the ones measured at large-signal conditions, ~1.5 mC/m^2 *vs.* ~25 mC/m^2. To explain this discrepancy one must consider the differences in switching mechanisms at small- and large-signal conditions. While the large-signal response reflects both reversible and irreversible polarization switching processes, the small-signal effects are mostly driven by reversible polarization modulations.[4] Irreversible changes are related to extrinsic phenomena as transitions between global energy minima (e.g. full polarization reversal between $+P_r$ and $-P_r$) and movement of ferroelectric domain walls; reversible effects arise from the dielectric response and intrinsic phenomena that are coupled to small fluctuations around local minimum potential points, such as ion displacement in perovskite ferroelectrics, or, in the case of amide-based ferroelectrics, columnar macrodipole rotation. The almost 20 times higher large-signal polarization in BTTTA-C12 implies that the macroscopic-extrinsic-irreversible, and not the microscopic-intrinsic-reversible mechanisms dominate the large-signal ferroelectric switching. This is similar to the behavior of benzene-cored analogues examined previously[5].

VI. Discussion of coercive fields in amide-based ferroelectrics

There are several microscopic and macroscopic conditions that affect coercive fields in amide-based ferroelectrics. Microscopic effects like intermolecular steric hindrance influence intrinsic energy barriers for single dipole flipping, while the macroscopic properties, such as a degree of cooperativity in molecular self-assembly and the typical size of supramolecular structures, determine extrinsic energy barriers.

We have recently shown that improved self-assembly and lower structural disorder leads to increased coercive fields. This effect was demonstrated by comparing linear- (hexyl to dodecyl tail) and branched-tailed (2-ethylhexyl and 1-hexylheptyl tail) BTAs, where 2–5 times higher coercive fields were found for the latter ones.[3] In this case of varying side-chain substitutions, intercolumnar/intermolecular electrostatic interactions and steric hindrance were found to be of lower importance, as concluded on basis of DFT/MD simulations. For **BTTTA**, as the alkyl side-chains are linear, any improvements in structural order and thereby an increase in coercive field must be related to the effect of a larger BTT core and concomitant stronger intermolecular π-π interactions. The effect may manifest itself at the macroscale as an enhanced self-assembly, and at the nanoscale as an increased energy barrier for dipole flipping.

The stronger core-core coupling in **BTTTA** facilitates supramolecular self-assembly, which we observed as strong gelation in solution.[6] Despite the different approaches of molecular engineering – mesogenic tail branching discussed above or increasing size of the conjugated core – the coercive field *vs.* temperature trends are very similar: compare the data for **BTTTA** and BTA-C6/2 (with 2-ethylhexyl tail) in Fig. S8c. Both materials demonstrated strongly enhanced self-assembly in solution. As discussed in more detail in the main text, larger supramolecular units increase extrinsic energy barriers for both field- and thermally-driven polarization switching.

The effect of larger, stronger-coupled cores on the microscopic dipole rotation barrier has not been investigated systematically in theory. However, DFT/MD studies on a different BTT-trisamide homologue find a helical pitch of 9 molecules[7] while 6 were found for benzene-trisamides[3], that is, BTTTA (BTA) cores are shifted by 40° (60°) with respect to each other in a helical self-assembled stack, see Figure S9a,b. The dihedral angle β between the amides and the core plane was calculated to be in range 37–40° for BTTTA and 42–46° for BTA[8]. As discussed in detail in the paragraph below, these molecular packing peculiarities strongly influence the nanoscopic polarization switching mechanisms through electrostatic interactions.

VII. Kinetic Monte Carlo Simulations of BTTTA

We have investigated the effect of the morphology on the nanoscopic polarization switching kinetics of BTTTA, using kinetic Monte Carlo simulations.[9] This model is purely electrostatic and ignores any steric effects and related rotational barriers. It reduces the molecules to a collection of point dipoles with a fixed position but variable orientation. The energies of all possible dipole flips are calculated based on electrostatic interactions. These energies are converted into flipping rates that are the input for a kinetic Monte Carlo algorithm. More details on this model can be found in Ref. 9. To allow a good comparison with BTA, all input parameters are the same as in Ref. 9, except for the morphological parameters that were adapted to reflect the morphology of BTTTA, as shown in the Table below.

Parameter	**Value BTTTA**	**Value BTA**	**Unit**
Helical pitch	9	6	molecules
OOP rotation β	40	60	degrees
Hexagonal packing distance a	3.5	1.67	nm
Interdisc distance c	0.35	0.35	nm
Dipole distance from center L	0.5	0.28	nm

When considering rotating dipoles, there are two different ways to reverse the polarization, as shown in Figure S9b. In the first flipping mode, the dipoles will flip in the *xy*-plane and only invert their *z*-component, which we call the ‘*z*-flip’. In the other flipping mode, the dipole vector will fully invert, which we call the ‘full flip’. It was found that in BTA the *z*-flip has a much lower coercive field and thereby is the dominant flipping mode.[9] However, for BTTTA, this *z*-flip does not exist. When all dipoles change their *z* component in BTTTA, this does not create a new triple helical hydrogen bonded network, in contrast to BTA. This is due to the aforementioned larger helical pitch and thereby smaller rotational angle between neighboring molecules.

The simulated hysteresis loops for both BTTTA and BTA are shown in Figure S9. The coercive field of BTTTA is larger than that of the *z*-flip mode in BTA, which is the favorable flipping mode for BTA. This difference in coercive field is likely caused by the difference in flipping mode. In the case of BTA, the full flip mode has a much larger coercive field than the *z*-flip mode. This is due to the unfavorable head-to-head interaction that arises from flipping one dipole in the full flip mode. Since BTTTA is restricted to the full flip mode, its coercive field is relatively high.

The fact that the coercive field of BTTTA is lower than the full flip mode of BTA, is likely because the dipoles in BTTTA are further away from the center and thereby from each other. This will reduce the cooperativity effect and thus the coercive field. If the *z*-flip was available for BTTTA, its coercive field would probably be lower than that of BTA. We note in passing that this suggests a design rule to simultaneously achieve low coercive field and high retention: materials with a large, well-stacking core having a 6-unit pitch would be expected to maintain the large structural order (and suppressed intra-columnar Coulomb interaction) of BTTTA while enabling the coercive field lowering z-flip.

To conclude this discussion, the high coercive field (and high retention) in BTTTA is likely a combination of three different mechanisms. First, BTTTA shows an improved self-assembly and structural order. Second, the energy barrier for dipole rotation due to steric effects is likely higher. Third, BTTTA is restricted to the full flip mode which has an inherently larger coercive field.

VIII. Refuting alternative resistive switching mechanisms

In case of bulk conductivity switching, no other frequency dependence than via E_c is expected when working at low frequencies ($f << 1/t_{sw}$), as the conductivity modulation effect is static in nature. Indeed, the current density does increase neither at the 'on' nor at the 'off' state with changing sweeping rate and the curves fall on the same fitted line of the space-charge limited conductivity (SCLC) (Fig. S12a):

$$j(V) = \frac{9}{8}\varepsilon_0\varepsilon_r\mu_0\frac{V^2}{d^3}\exp\left(0.891\gamma\sqrt{V/d}\right). \qquad \text{(Eq. S1)}$$

Here V is the applied voltage, d is the layer thickness, μ_0 is the zero-field mobility, γ is a phenomenological parameter quantifying the mobility enhancement by the applied electric field and $\varepsilon_0\varepsilon_r$ is dielectric permittivity of the material. This confirms the non-transient character of the mechanism. The integrated charge is also much larger than the polarization charge, which proves that it is not the switching current dP/dt that is measured. Electrochemical reactions can also be refuted as the loops do not grow at slower sweeping speeds[10] and in general are very reproducible and stable with time. Ionic activity is unlikely to be responsible for the effect as ion transport happens at much lower characteristic fields, especially at elevated temperatures.[11] Transient doping and charge trapping-detrapping can also be ruled out because of different typical form of J-V characteristics[12] and also because no change in layer color was observed. Effect of hot electrode deposition and consequent formation of dead layers at the interface is unlikely, as similar behavior was observed in 'cold' in-plane interdigitated gold electrode devices with 5 μm gap, see Fig. S13 and Section IX.

IX. In-plane devices

Interestingly, notably higher current densities (~1 mA/cm^2) and SCLC mobilities (~10^{-4} cm^2/V/s) were found in in-plane devices, see Fig. S13. For device preparation details see Section II. These values are close to the photogenerated charge mobility of ~10^{-3} cm^2/V/s found for analogous to the BTTTA material in shear-aligned samples in a lyotropic phase.[7] The reason to this improvement may lie in better molecular alignment with respect to the electric field. After deposition from solution (with molecularly dissolved material), molecules self-assemble in stacks that lie in-plane to the substrate, which strongly favors the in-plane device geometry[13]. Homeotropic alignment for out-of-plane devices is achieved by a short field-annealing procedure at lower viscosity conditions.[3] For this, initial self-assembled structures must be broken up and reformed to follow the field lines. This field-alignment approach has been shown to be very effective in small benzene-cored amide-based ferroelectrics. However, due to the large BTT cores and long initial supramolecular assemblies held together by strong intermolecular interactions, this field-assisted rearrangement of molecules may not be efficient. This might also be a reason for the previously reported hardship to observe bulk ferroelectricity and conductivity switching in the carbonyl-bridged triarylamine-based α-CBT material in out-of-plane geometry devices.[14]

X. Dynamic double-switching regime

We have prepared and tested different injecting electrode materials and structures that all gave similar results as the Au/Al devices presented in Fig. 3b of the main text (bottom electrode / top electrode): Al/MoOx:Al, MoOx:Al/Al, Al:MoOx/MoOx:Al, ITO:PEDOT/Al. The behavior is independent of electrode material and electrode arrangement (top/bottom or bottom/top, which could give rise to differences in thermal impact and resultant ‘dead’ layers), which proves that electrode-induced or ionic artefacts are not present.

Devices with one blocking and one injecting electrode, see Fig. S14, are convenient to simultaneously observe the polarization switching (reverse) current dP/dt and the charge transport (forward) current and, in future devices, allow to mitigate crosstalk problems present in crossbar array memory structures. We plot the reverse and forward bias response of a representative device on the same absolute field axis to be able to compare the behavior in these diode structure devices.

XI. Supplementary figures

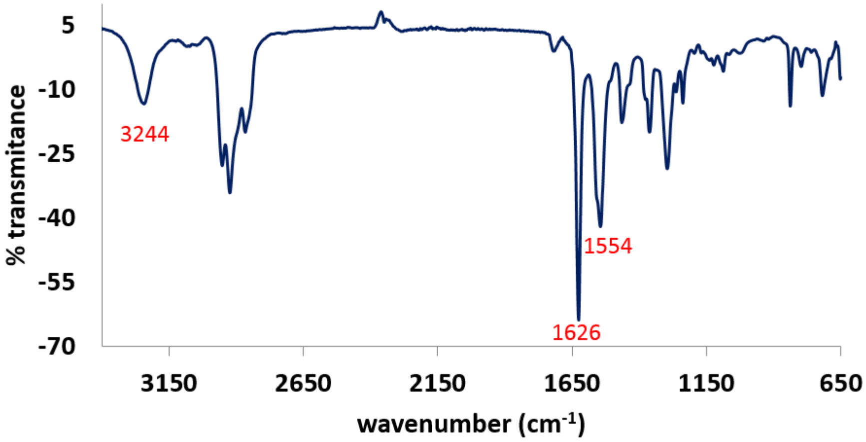

Figure S1. Infrared spectrum (IR) of **BTTTA** presenting N-H vibrations around 3244 cm-1 and amide vibrations at 1626 and 1554 cm^{-1} in the solid state.

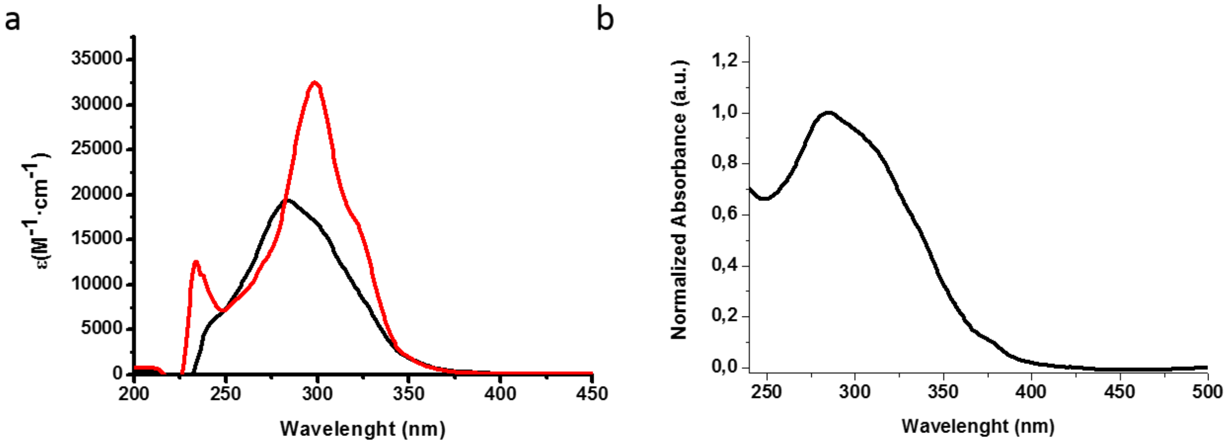

Figure S2. UV spectra of BTTTA: (a) In the aggregated form in chloroform (c = 2.5x10^{-5}M) at 25ºC (black line) and in the molecularly dissolved state in THF (red line) where it is possible to see the difference between monomer and aggregates. (b) In the aggregated state on quartz substrates spin coated from a solution in chloroform (c = 1.0x10^{-4}M).

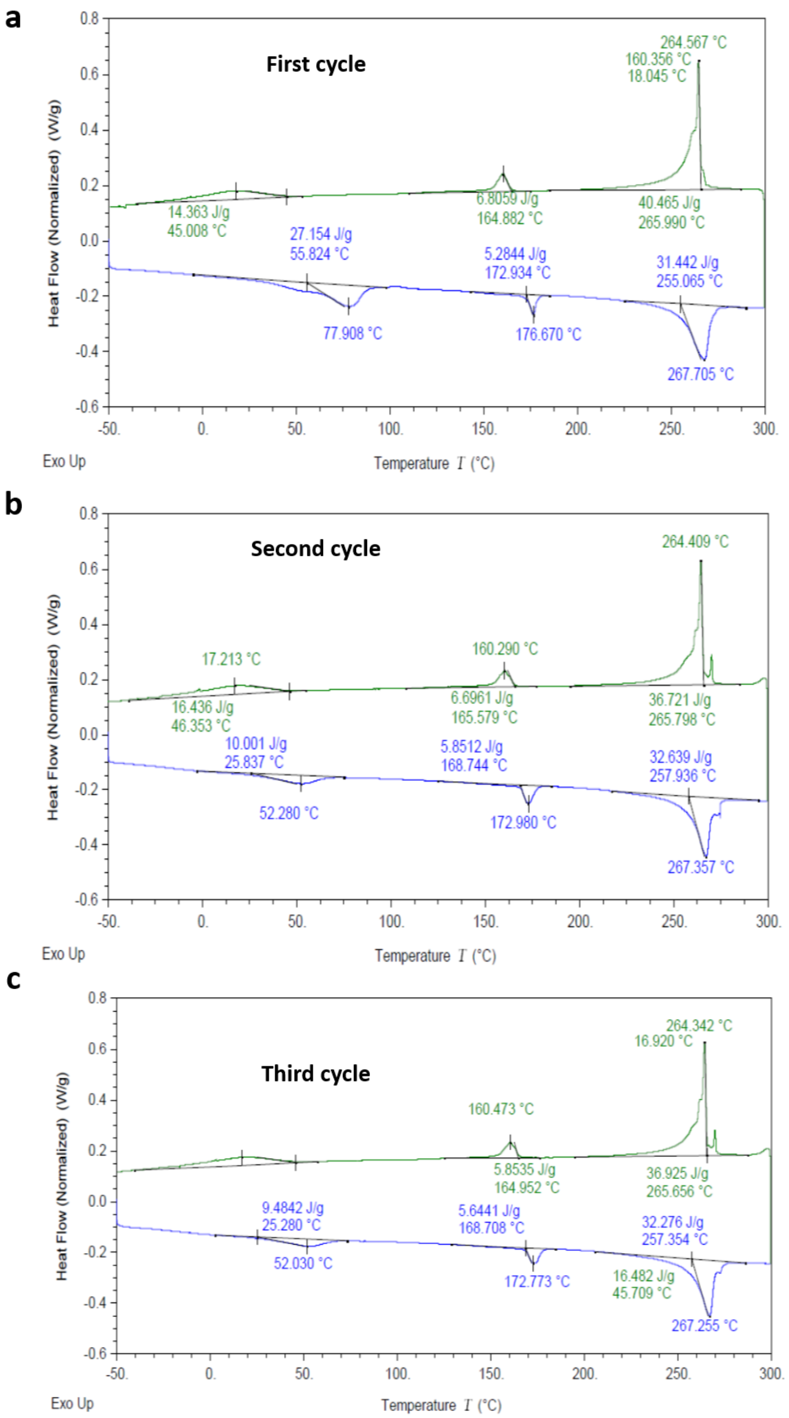

Figure S3. DSC traces of **BTTTA** (heating and cooling rate = 10 °C/min, right). (a) 1st heating run. (b) 2nd heating run. (c) 3rd heating run.

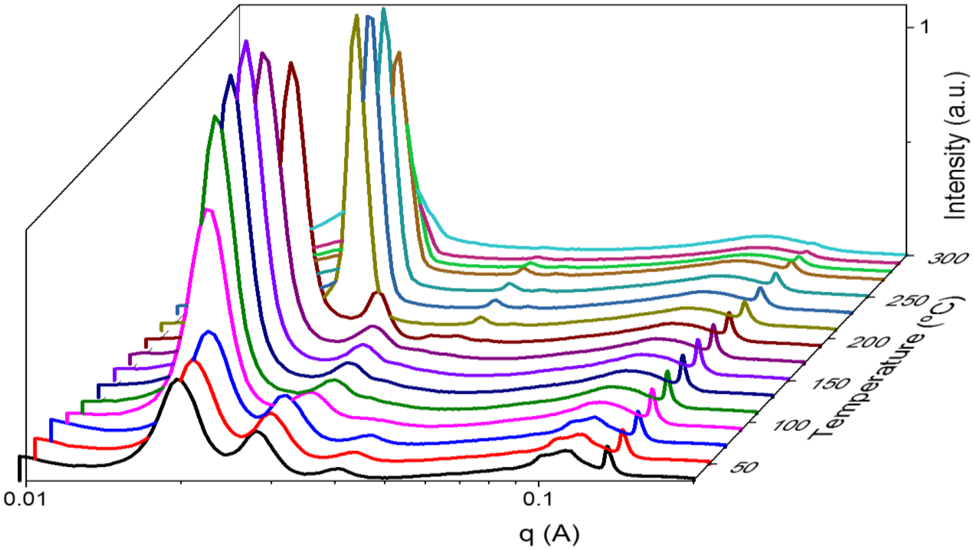

Figure S4. TD-WAXS spectra. The sample of **BTTTA** was placed in a glass capillary and the WAXS profiles were measured at regular intervals in the 300 ºC-30 ºC temperature range upon cooling at 10 ºC/min.

	25ºC			**140ºC**			**220ºC**		
hkl	***q* (nm^{-1})**	**d_{obs} (nm)**	**d_{cal} (nm)**	***q* (nm^{-1})**	**d_{obs} (nm)**	**d_{cal} (nm)**	***q* (nm^{-1})**	**d_{obs} (nm)**	**d_{cal} (nm)**
100	2.72	2.31	2,30	1.18	3.39	3.39	2.29	2.73	2.73
110	3.85	1.63	1.63	2.62	2.40	2.40	4.02	1.56	1.58
200	5.41	1.16	1.15	3.64	1.73	1.71	4.64	1.36	1.36
Aliphatic halo	15.0	0.42	-	10.44	0.57	-	10.4	0.60	-
Interdisc	18.1	0.35	-	17.2	0.37	-	15.2	0.41	-
Intercolumn	-	2.31	-	-	3.39	-	-	3.16	-
Lattice	Crystalline Col$_{tet}$ (*p4mm*) a = b = 2.31; c = 0.35 nm			Mesophase Col$_{tet}$ (*p4mm*) a = b = 3.39; c = 0.37 nm			Mesophase Col$_{hex}$ (*p6mm*) a = b = 3.16; c = 0.41 nm		

Table S1. Summary of the *d*-spacings (nm) corresponding to the peak positions (d_{obs} = *d* observed, d_{cal} = *d* calculated) and LC mesophases of **BTTTA** at 25 ˚C, 140 ˚C and 220 ˚C derived from Figure S4.

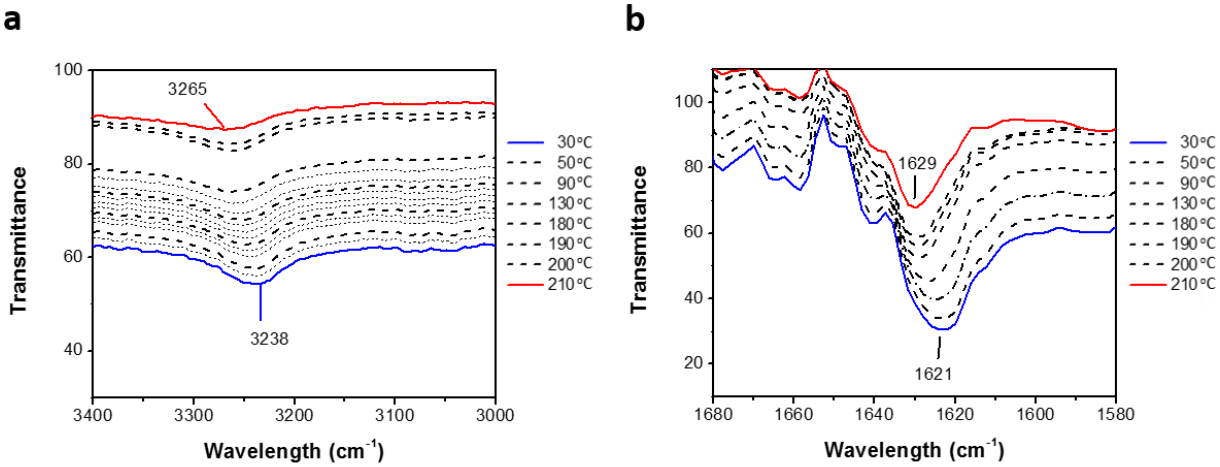

Figure S5. TD-IR spectra upon heating from 30 °C to 210 °C of **BTTTA**, heating rate (10 ºC/min) a) N-H stretching. (b) Amide I vibration.

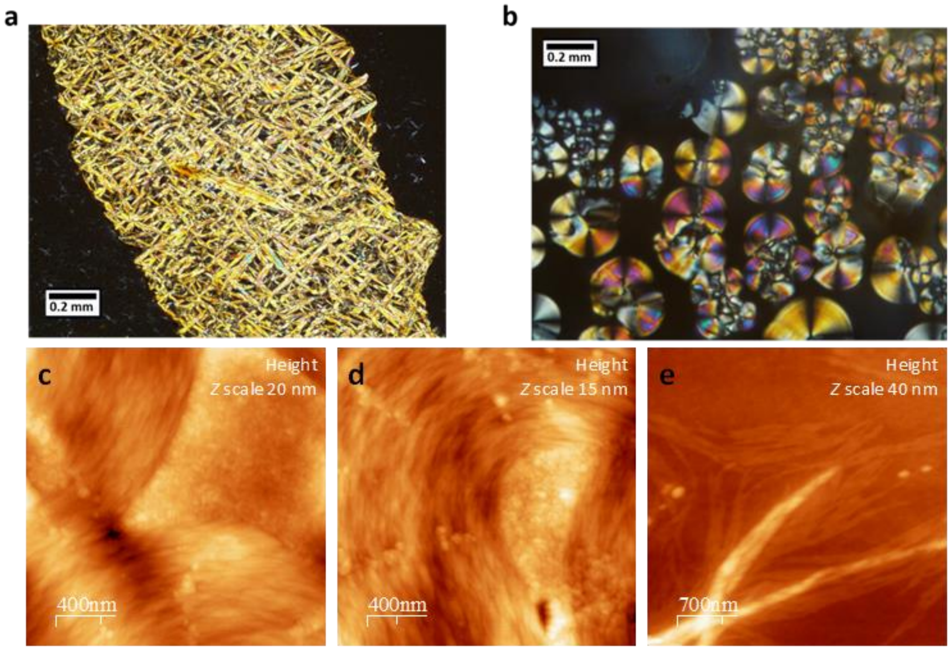

Figure S6. POM micrographs after cooling from the isotropic melt (cooling rate 10 °C/min) at a) 10°C and b) 240°C. (c–e) AFM images of (c,d) annealed spin-coated **BTTTA** films from concentrated chloroform gels and (e) from diluted toluene solution, with clearly visible self-assembled supramolecular aggregates.

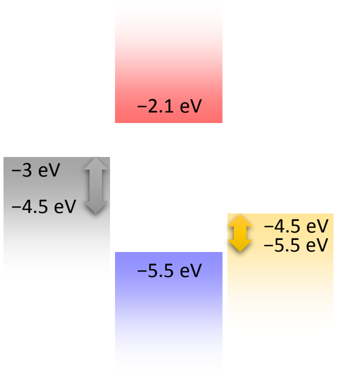

Figure S7. Energy diagram of BTTTA. A range of work-functions for blocking (Al, Al:LiF, left) and injecting electrodes (Au, ITO, PEDOT:PSS, MoOx:Al) are given for reference.

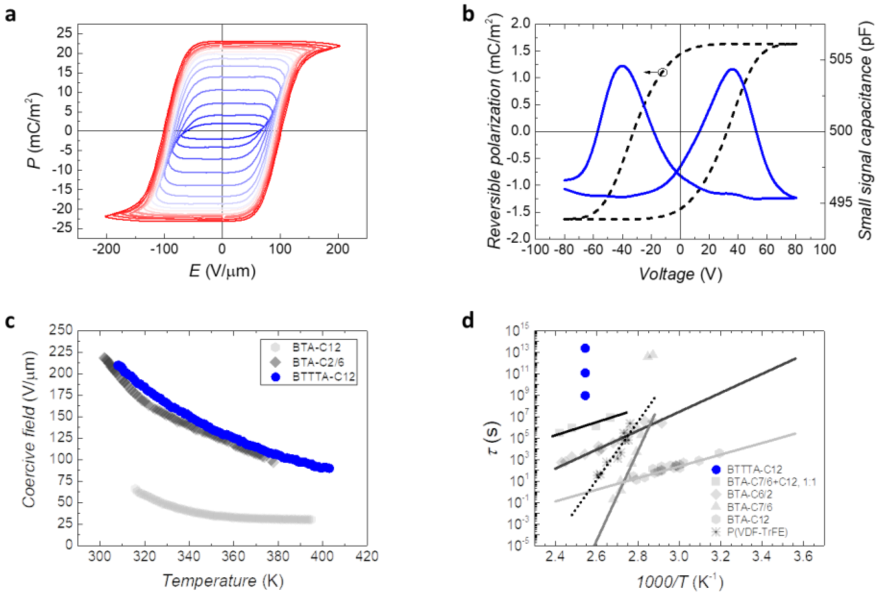

Figure S8. Ferroelectric characteristics measured on devices with both blocking aluminum electrodes. (a) Polarization saturation with increasing applied electric field, data obtained at 120°C, 25 Hz. (b) Capacitance-voltage (blue solid line) characteristics measured at 120°C, 1 kHz small-signal frequency. A black dashed line represents the integrated *C-V* butterfly loop, resulting in a reversible polarization, which is significantly lower compared to the large-signal macroscopic polarization of ~25 mC/m^2 and implies that reversible/intrinsic/microscopic switching is not dominating the large-signal response. Here, a linear dielectric response was subtracted after integration. (c) Coercive field dependence on temperature, measured at 25 Hz applied field frequency for BTTTA (blue symbols) and compared to benzene-cored analogues BTA-C12[2] and BTA-C6/2[3]. Extrapolation gives the 0 K intrinsic coercive field at 25 Hz of around 600 V/µm. (d) Arrhenius plot for depolarization activation. Data for different samples of BTTTA is marked in blue, for BTA homologues and P(VDF-TrFE)[3] – as marked in the legend.

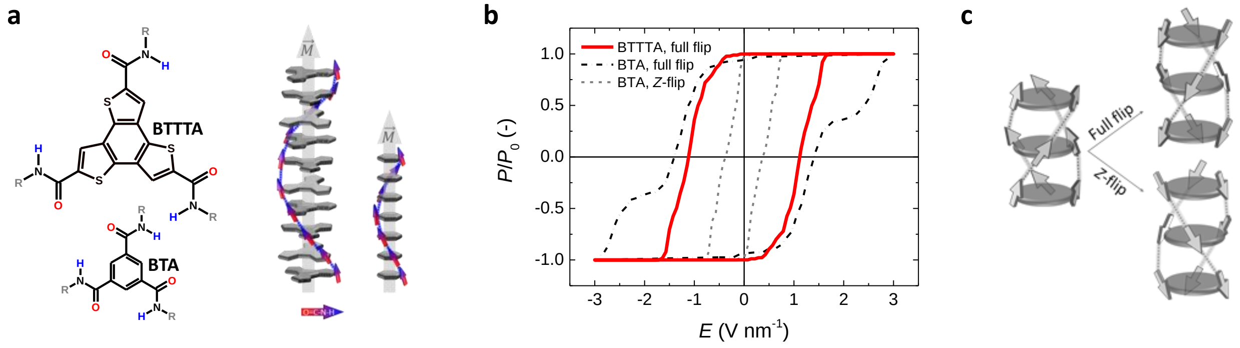

Figure S9. Hysteresis loops simulated using kinetic Monte Carlo calculations. (a) Different axial molecular packing for BTTTA and BTA, corresponding to the helical pitch of 9 and 6 molecules, respectively. (b) The normalized hysteresis loops for both possible flipping modes of BTA and the full flip mode of BTTTA, simulated at 250 Hz and 325 K. (c) The corresponding two flipping modes, schematically shown for the BTA molecule. Due to the larger helical pitch of BTTTA, the z-flip mode is not possible for this compound.

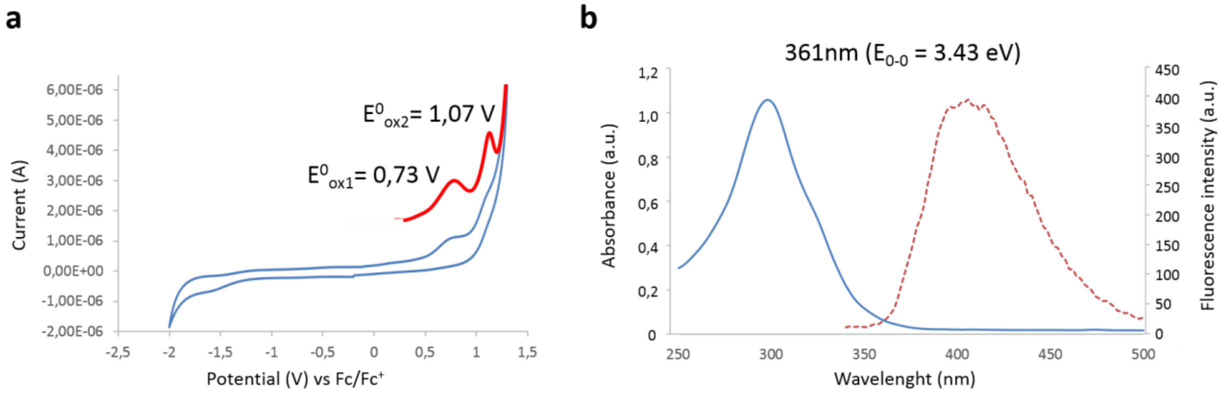

Figure S10. a) Cyclic voltammogram of BTTTA. Potential values are registered vs Ag/AgNO$_3$ reference electrode, inset: Square Wave Voltammetry (SWV) (red line); b) Absorption (solid line) and fluorescence spectra (dashed line) of BTTTA (excitation wavelength, 287 nm). The HOMO energy level was obtained using the approximation $E_{\text{HOMO}} = -4.8 - E_{\text{ox}}^{1/2}$ (vs Fc/Fc$^+$) $= -5.5$ eV. The LUMO energy level was obtained by using optical ($E_{0\text{-}0}$) bandgap obtained from the interception between the absorption and emission spectra $E_{\text{LUMO}} = E_{\text{HOMO}} + E_{0\text{-}0} = -2.1$ eV.

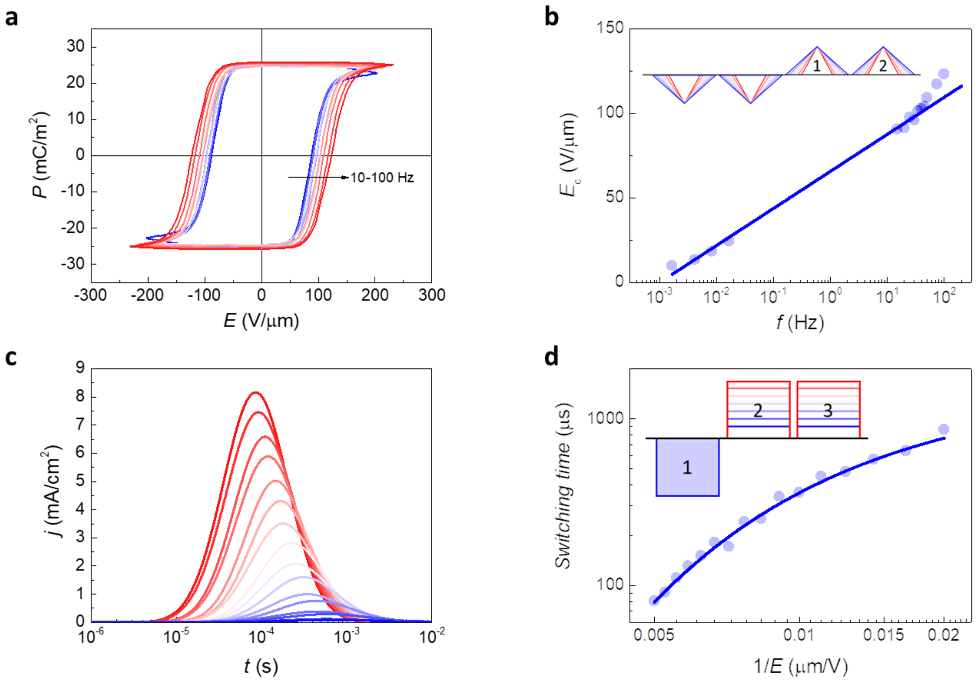

Figure S11. Dynamic ferroelectric switching characteristics measured on devices with blocking aluminum electrodes. (a) *P*-*E* characteristics versus the applied field sweeping frequency using a triangular input signal (inset of panel (b), step 1 – switching-current, step 2 – non-switching background current probing), measured at 120°C. The corresponding coercive field *vs.* frequency trend is given in (b) and fits well to the thermally-activated nucleation-limited switching model: $E_\mathrm{c} \cong \frac{w_\mathrm{b}}{P_\mathrm{r}} - \frac{k_\mathrm{B}T \cdot \ln\left(\nu_0/f \cdot (\ln(2))^{-1}\right)}{P_\mathrm{r}V^*}$ with a critical nucleus volume for polarization switching $V^* = 23$ nm^3, and the characteristic activation energy density $w_\mathrm{b} = 0.05$ eV/nm^3 leading to a total energy barrier for switching W_b of 1.15 eV (solid line). Note that for BTAs a nucleus volume $V^* \approx 6$ nm^3 is typically found, consistent with the superior retention in the BTTTA material.[8] Low-frequency points around 10^{-3} – 10^{-2} Hz come from the quasi-static *J*-*V* curves in Fig. 3a. (c) Polarization switching current transients for increasing applied electric field (from blue to red), measured at 120°C. The polarization switching time (i.e. time coordinates of the current transient peak positions) dependence on the reciprocal field is given in (d) and fits well to the same thermally-activated nucleation-limited switching model $t_\mathrm{sw} \cong \frac{1}{\nu_0} \cdot \exp\left(\frac{(w_\mathrm{b} - P_\mathrm{r}E_\mathrm{app})V^*}{k_\mathrm{B}T}\right)$ with similar parameters as given above (blue line). Inset: measurement scheme, where preparation step 1 is used to erase previous polarization states; polarization switching kinetics is measured at step 2 from which the non-switching background measured at step 3 is subtracted.

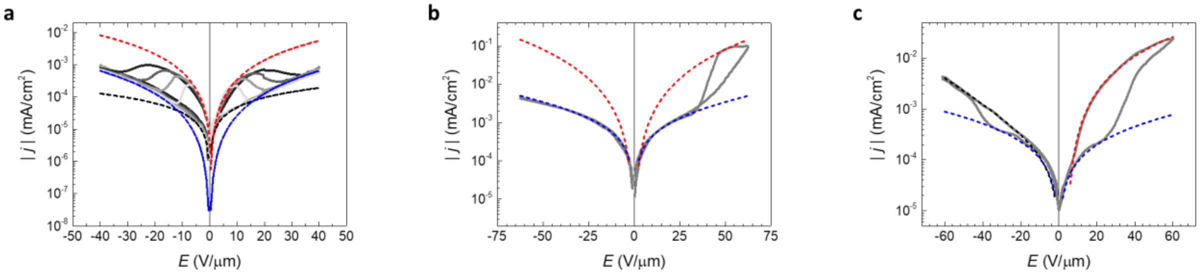

Figure S12. Fitting of the *J*-*V* curves of Fig. 4 of the main text to the SCLC expression, Eq. S1. (a) Bulk conductivity switching (BCS): SCLC 'on' state (red line) with $\mu_0 = 1.5 \cdot 10^{-9}$ cm^2/V/s, $\gamma = 0$; SCLC 'off' state (blue line) with $\mu_0 = 1 \cdot 10^{-10}$ cm^2/V/s, $\gamma = 0$; Ohmic region (black line) with unintentional doping level $n_0 = 10^{15}$ cm^{-3} (b) Hybrid regime (BCS+IBM): SCLC 'on' state (red line) with $\mu_0 = 2.1 \cdot 10^{-8}$ cm^2/V/s, $\gamma = 0$; ILC 'off' state (blue line), exponential function. (c) Injection barrier modulation (IBM): SCLC 'on' state (red line) with $\mu_0 = 1.7 \cdot 10^{-8}$ cm^2/V/s, $\gamma = 0.002$ (cm/V)$^{0.5}$; ILC 'off' state (blue line) exponential function; ILC 'on' state (black line) exponential function. Relative permittivity $\varepsilon_r = 3.5$ was used for fitting.

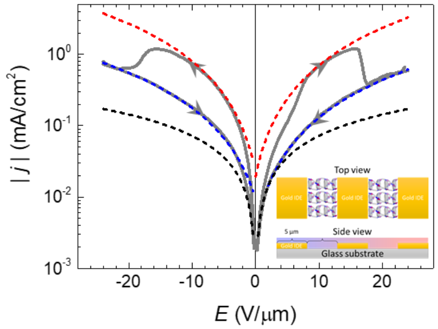

Figure S13. Bulk conductivity switching *j*-*E* characteristics of a spin-coated in-plane interdigitated gold electrode device (scheme given as inset). In this geometry molecular stacks are largely aligned along the field lines – perpendicular to the electrodes, which results in higher fitted SCLC charge transport mobilities, compared to the out-of-plane devices. Here, SCLC 'on' state (red line) with $\mu_0 = 7\text{–}8 \cdot 10^{-5}$ cm^2/V/s, $\gamma = 0$; SCLC 'off' state (blue line) with $\mu_0 = 1.3\text{–}1.5 \cdot 10^{-5}$ cm^2/V/s, $\gamma = 0$; Ohmic region (black line) with unintentional doping level $n_0 = 10^{15}$ cm^{-3}.

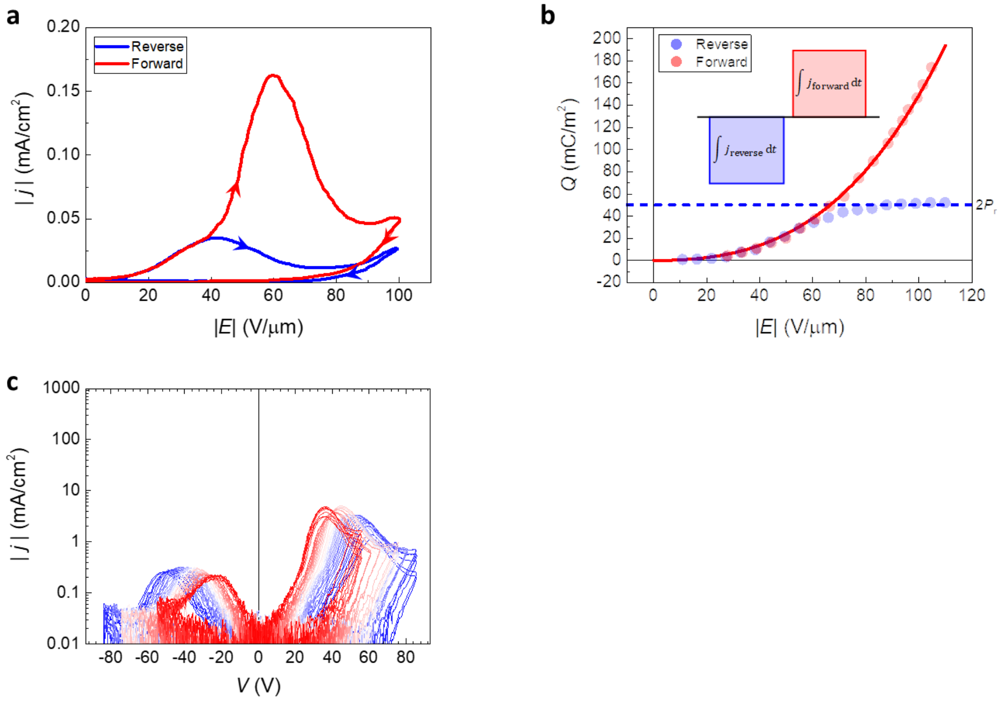

Figure S14. High-frequency *j-E* characteristics of Al/BTTTA/MoOx:Al device showing the double resistive switching regime. (a) *j-E* curves for reverse (only polarization switching, +Al) and forward (polarization switching and injected charges, +MoOx:Al) bias, measured at 10 Hz triangular field signal. (b) Integrated transported charge, measured at quasi-static conditions (as in inset) on a similar device at forward (data in red) and reverse (data in blue) bias. The red line is a fit to the SCLC expression Eq. S1 with $\mu_0 = 1.3 \cdot 10^{-9}$ cm^2/V/s, $\gamma = 0.002$ (cm/V)$^{0.5}$. The blue line sits at the double remnant polarization of the ferroelectric. The probing pulse length was 20 ms. (c) The switching behavior is stable over a broad temperature range, from 125°C to room temperature and below (+MoOx:Al, aluminum electrode grounded).

References

1 A. V Gorbunov, M. García-Iglesias, J. Guilleme, T. D. Cornelissen, W. S. C. Roelofs, T. Torres, D. González-Rodríguez, E. W. Meijer, M. Kemerink, *Sci. Adv.*, 2017, **3**, e1701017.

2 I. Urbanaviciute, X.Meng, T. D. Cornelissen, A. V. Gorbunov, S. Bhattacharjee, R. P. Sijbesma and M. Kemerink, *Adv. Electron. Mater.* 2017, **3**, 1600530.

3 I. Urbanaviciute, S. Bhattacharjee, M. Biler, J. A. M. Lugger, T. D. Cornelissen, P. Norman, M. Linares, R. P. Sijbesma and M. Kemerink, *Phys. Chem. Chem. Phys.*, 2019, **21**, 2069.

4 D. Bolten, U. Böttger and R. Waser, *J. Eur. Ceram. Soc.*, 2004, **24**, 725.

5 I. Urbanaviciute *et al.*, Negative piezoelectric effect in an organic supramolecular ferroelectric, *Under review*, 2019.

6 S. S. Babu, S. Prasanthkumar, A. Ajayaghosh, *Angew. Chem. Int. Ed.*, 2012, **51**, 1766.

7 A. Demenev, S. H. Eichhorn, T. Taerum, D. F. Perepichka, S. Patwardhan, F. C. Grozema, L. D. A. Siebbeles and R. Klenkler, *Chem. Mater.*, 2010, **22**, 1420.

8 C. Kulkarni, S. K. Reddy, S. J. George, S. Balasubramanian, *Chem. Phys. Lett.*, 2011, **515**, 226.

9 T. D. Cornelissen, M. Biler, I. Urbanavičiūtė, P. Norman, M. Linares and M. Kemerink, *Phys. Chem. Chem. Phys.*, 2019, **21**, 1375.

10 X. Meng, A. V. Gorbunov, W. S. Christian Roelofs, S. C. J. Meskers, R. A. J. Janssen, M. Kemerink and R. P. Sijbesma, *J. Polym. Sci. Part B Polym. Phys.*, 2017, **55**, 673.

11 L. Müller, S.-Y Rhim, V. Sivanesan, D. Wang, S. Hietzschold, P. Reiser, E. Mankel, S. Beck, S. Barlow, S. R. Marder, A. Pucci, W. Kowalsky, R. Lovrincic, *Adv.Mater.*, 2017, **29**, 1701466.

12 X. Zou, H. Guan Ong, L. You, W. Chen, H. Ding, H. Funakubo, L. Chen, J. Wang, *AIP Adv.*, 2012, **2**, 032166.

13 A. Demenev, S. H. Eichhorn, T. Taerum, D. F. Perepichka, S. Patwardhan, F. C. Grozema, L. D. A. Siebbeles and R. Klenkler, *Chem. Mater.*, 2010, **22**, 1420.

14 C. F. C. Fitie, W. S. C. Roelofs, M. Kemerink and R. P. Sijbesma, *J. Am. Chem. Soc.*,2010, **132**, 6892.